2017-24-0019

The Sensitivity of Transient Response Prediction of a Turbocharged Diesel Engine to Turbine Map Extrapolation

Author, co-author (Do NOT enter this information. It will be pulled from participant tab in MyTechZone)

Affiliation (Do NOT enter this information. It will be pulled from participant tab in MyTechZone)

Abstract

Mandated pollutant emission levels are shifting light-duty vehicles towards hybrid and electric powertrains. Heavy-duty applications, on the other hand, will continue to rely on internal combustion engines for the foreseeable future. Hence there remain clear environmental and economic reasons to further decrease IC engine emissions. Turbocharged diesels are the mainstay prime mover for heavy-duty vehicles and industrial machines, and transient performance is integral to maximizing productivity, while minimizing work cycle fuel consumption and CO2 emissions.

1D engine simulation tools are commonplace for “virtual” performance development, saving time and cost, and enabling product and emissions legislation cycles to be met. A known limitation however, is the predictive capability of the turbocharger turbine sub-model in these tools. One specific concern is accurate extrapolation of turbine performance beyond the narrow region populated by supplier-measured data to simulate non-steady conditions, be it either to capture pulsating exhaust flow or, as is the focus here, engine transient events. Extrapolation may be achieved mathematically or by using physics-based correlations, sometimes in combination. Often these extrapolation rules are the result of experience. Due to air system dynamic imbalance, engine transients force instantaneous turbine mass flow and pressure ratio into regions well away from the hot gas bench test data, necessitating great trust in the extrapolation routine.

In this study, a 1D heavy-duty turbocharged diesel engine model was used to simulate four transient events, employing a series of performance maps representing the same turbine but with increasing levels of extrapolation, using commonly-adopted methodologies. The comparison was enabled by measuring real turbine performance on the dynamometer at Imperial College London. This testing generated a wide baseline dataset which was used to produce corresponding transient response predictions, and against which cases of increasing degrees of extrapolation could be compared. This paper studies the sensitivity of response time to the degree and technique of the extrapolation applied, demonstrating its importance for reliable transient engine simulations.

Introduction

The use of software tools for virtual product engineering has become commonplace in the automotive industry since it accelerates product cycles while at the same time accommodating increasingly complex technological requirements. The goal is to reduce the requirement for physical testing, which is expensive and time consuming, to an absolute minimum. This need is becoming recognized and, for instance, the Automotive Council UK is targeting a 70% virtual validation by 2025 [1]. This, of course, implies the availability of software models of sufficient accuracy.

One area in which virtual product engineering is applied to the development of turbocharged diesel engines is through the use of 1D engine cycle simulations tools. CAT® off-road machines operate complex duty cycles with rapid transitions between multiple states of engine speed and load. Accurate prediction of transient response is therefore crucial for gaining insight into engine performance and emissions over such duty cycles, as early in the development process as possible (thereby reducing the need for physical testing later). Realistic simulation of the engine air system is a major determining factor. Within the air system, the turbocharger turbine sub-model is of considerable interest, irrespective of the particular software package, due to the difficulties in predicting turbine operation and the consequent need to supply empirical data to characterize its performance.

During an engine acceleration event, the engine crankshaft is loaded much more quickly than the turbocharger, as the engine rapidly burns additional fuel without exceeding the smoke limit. This rapid torque increase is called ‘snap torque’. The coupling between the engine and the turbocharger is fluid dynamic, as opposed to mechanical, and there is therefore an inherent delay in the spooling of the turbocharger, commonly known as ‘turbo lag’. Since the turbocharger compressor supplies the engine cylinders with pressurized air, the transient response (TR) is a system effect, and can only be predicted by taking into account the unique combination of engine and turbocharger under consideration.

Engine transients can fall into a number of categories, denoting such aspects as whether the engine is accelerating or decelerating, the way in which the speed varies with the torque, the parameter of interest (speed, torque, power, fuel flow etc.), and other properties. In a similar vein, various test specifications exist to characterize the engine for these different scenarios. The two transients featured in this study are the torque converter stall (TCS) and the constant speed load acceptance (CSLA). The TCS transient replicates the engine together with a torque converter installed in the driveline, while the CSLA is performed on a dynamometer, from low load to full load with the engine speed held constant.

In 1D engine simulation codes, common practice is to represent the turbocharger performance via the use of performance maps, which relate the pseudo-nondimensional parameters of reduced mass flow rate (MFR), reduced shaft speed, pressure ratio (PR) and efficiency, in a standardized “SAE” map. Turbocharger manufacturers provide measured data maps in this format, typically recorded on hot gas stands where the boundary conditions are controlled using a fuel burner and various control valves and measurement sections [2]. The turbines are almost always tested as part of the turbocharger unit, meaning that the compressor must act as the turbine brake, and this limits the range of operating points attainable without pushing the compressor into the surge and choke regions. Furthermore, the turbochargers are tested under steady conditions. Watson [3] explains

how this constitutes an additional source of error in transient response prediction, since the assumption of quasi-steady flow is not valid for the turbine during transient events. Pulsating engine exhaust flows combined with transient engine cycle-averaged power give rise to operation of the turbocharger at pressure ratios and reduced mass flow rates far outside of the range of data typically obtainable in these characterization tests – an example showing a torque converter stall is shown in Figure 1. Some authors (see [4]) have demonstrated increased turbine measurement range on the gas stand by adjusting the turbine inlet temperature (TIT), or pumping compressed air into the compressor to increase its power consumption, amongst other adjustments. If turbocharger manufacturers were to adopt these techniques alongside the standard practices, they could provide turbine maps whose speed lines were extended at both ends on the reduced MFR – PR axes. However, the range of pressure ratios experienced by a turbocharger turbine on-engine during a transient event at any given turbocharger speed is still outside of this extended range. Simulation of typical engine duty cycles therefore still necessitates the extrapolation of the measured performance data, to model the turbine off-design. As will be seen a variety of techniques have been developed to address this problem; some physics-based [5], others numerical [6,7], and some combinations of both [8]. It seems pertinent to expect that different modelling strategies, test rig setups, data integrity and coverage of the measured data, ought to affect predicted cycle-to-cycle engine performance during a transient.

While there are well-known commercially available 1D engine simulation tools, the current paper uses the Caterpillar Inc. Dynasty™ program to evaluate the impact of turbine map extrapolation on the transient response prediction of a heavy-duty diesel engine during various transient events. In the remainder of this paper, a more detailed overview of turbine modelling approaches in the literature is given, followed by the method of characterization of the turbine featured in this work. After this the procedures for creating the test maps are outlined, followed by a note on the 1D engine modelling software, the engine model used to simulate the transients, and the specifics of the transient events. The results of the study are then provided together with a discussion of the most important and most interesting outcomes. Finally, the conclusions of the study are given.

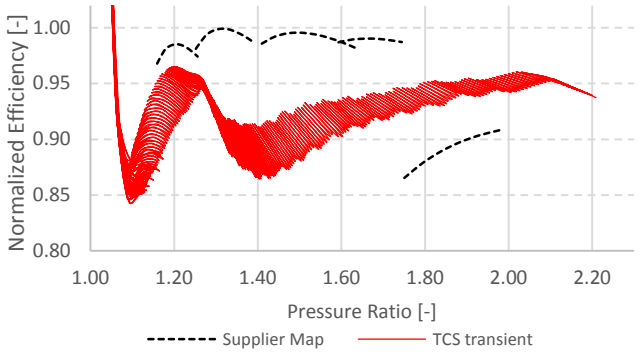

Figure 1. A torque converter stall transient overlaid on the SAE format supplier map from which it was simulated

Background to Turbine Modelling

Turbocharger turbine mass flow rates (*MFR*) and rotational speeds (*N*) are conventionally presented in reduced form,

$$\dot{m}_{\text{red}} = \dot{m}\sqrt{T_{0,\text{in}}}/p_{0,\text{in}} \tag{1}$$

$$N_{\text{red}} = N/\sqrt{T_{0,\text{in}}} \tag{2}$$

where $T_{0,in}$ and $p_{0,\text{in}}$ are the stagnation temperature and pressure at turbine inlet. This allows for the comparison of units tested under different inlet conditions, but not of different wheel diameters. The physical representation of the turbine flow regime can be simplified by analogy with a flow restriction. The mass flow rate through an orifice comes from compressible flow theory, but to describe a turbine, the orifice area is replaced with an *effective* area, A_{eff}:

$$\dot{m} = A_{\text{eff}}\sqrt{\gamma/R}\,\pi^{1/\gamma}\sqrt{\frac{2}{\gamma-1}\cdot\left[1-\pi^{\frac{\gamma-1}{\gamma}}\right]} \tag{3}$$

A key difference between a flow restriction and an IRF turbine is in the changing relationship between $\dot{m}_{\text{red}}$ and π as the turbine rotor speed increases. Inspection of any IRF turbine map will reveal the reducing magnitude of $\dot{m}_{\text{red}}$ for successive speed lines, which is due to the centrifugal pressure field set up in the rotor passages, and varies with the square of the rotational speed N_{red}. Thus, in a restriction analogy, A_{eff} ought to change according to the turbocharger speed. Watson [3] mentions that given sufficient details of the geometry of the turbine, the centrifugal pressure ratio can be calculated with relative ease and the point corresponding to the zero mass flow pressure gradient can be added to the supplier map, improving the starting information for extrapolation.

The turbine efficiency is often evaluated with respect to a different variable, the blade speed ratio (BSR),

$$\nu = \frac{U_{\text{t}}}{C_{is}} = \frac{(2\pi/60)\cdot ND}{\sqrt{2c_p\left(1-\pi_t^{\frac{\gamma-1}{\gamma}}\right)}} \tag{4}$$

In this way, the speed lines all collapse onto a family of very similar curves as exemplified in Figure 2. The BSR is a measure of blade loading. Plotting against the BSR reduces the error in extrapolation into regions of very high speed and low expansion ratio [3]. The variation of turbine efficiency with the BSR is due to multiple effects such as incidence, friction losses and tip clearance losses, which influence the most accurate A_{eff} to use in such a model. It is thus in the complexity of the function used to describe A_{eff} in terms of different turbine operating states, that the various flow extrapolation models diverge. Watson and Janota [9] and Benson [10] used a constant A_{eff} for all conditions, whilst Payri et al [11] allowed for changes in A_{eff} with N_{red} and PR, deriving a relation in which A_{eff} varies exponentially with BSR. Intermediate approaches have been proposed by El Hadef [5,12] and Martin [8], and [13]. In the former cases, a purely numerical model is developed for A_{eff}, whose coefficients are fitted polynomial functions with the PR. In the latter, a simple linear variation of A_{eff} with the BSR is adopted.

Eriksson [6] points out that an IRF turbine strictly comprises a throat in series with an impeller, and the impeller extracts work from the fluid, changing the choking characteristics of the turbine. This effect may be replicated in the restriction model, by a constant reduced MFR condition beyond the choking pressure ratio, $\pi_{\text{t,c}}$.

The accuracy of the flow restriction model is further hindered by the presence of heat transfer effects [14] which render the expansion through the turbine non-adiabatic. The isentropic flow equations are then strictly redundant. This amongst other phenomena raised above, gives rise to the universal necessity to adopt fitting constants in the extrapolation models to obtain a closer match to the data.

Efficiency models typically employ a quadratic variation of efficiency with BSR (Figure 2), with the general form,

$$\eta = -f(\nu^2) \tag{5}$$

to which constants and additional functions of ν raised to different powers may be added to improve the fit.

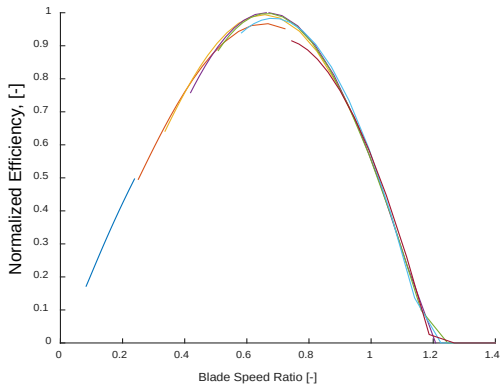

Figure 2. Normalized efficiency variation with BSR for a group of speed lines

Methodology

Turbine Performance Maps

The standard turbine map format [2,15] uses four columns for each speed (commonly four to ten speeds) – reduced speed, N_{red}, reduced MFR, $\dot{m}_{\mathrm{red}}$, PR, π_t, and total-to-static efficiency, η_{ts}. Hereon, all such variables refer to the turbine, unless specified otherwise.

Wide Mapping of the Test Turbine

The test turbine selected for this study is a Caterpillar-proprietary single entry IRF design, due to the availability of a high quality experimental dataset, measured using the cold-flow turbine dynamometer at Imperial College. This dataset was needed in order to compare simulation results for cases with different levels of extrapolation. The turbine loading device was a bespoke eddy current dynamometer [16], enabling measurement over a wide range of velocity ratio conditions since it is not constrained by compressor surge and choke, as would be the case for a traditional turbocharger hot gas bench. This results in performance characteristics that are typically at least three times as wide as those normally supplied, with consequently much less need for map extrapolation.

Modified Maps

Figure 3 shows the extent of the measured map data for the selected turbine, as reduced MFR against PR. Since no 'supplier' map exists for this turbine, a method was required to extract a set of starting points whose coverage and distribution would be similar to that measured on a hot gas stand. This dataset will be referred to as the supplier-width (SW) map. There are various means to do this (e.g., use turbocharger gas stand model with matched compressor, and record the turbine PR when the simulation flags supplier compressor surge or choke) but here, the turbine map data were recast into units that could be compared with other supplier maps, as follows.

The rate of gas enthalpy change through the turbine is

$$\dot{h}_{\mathrm{t}} = \dot{m}_{\mathrm{t}} c_{\mathrm{p}} \eta_{\mathrm{ts}} T_{0,\mathrm{in}} \left[1 - \pi_{\mathrm{t}}^{-\frac{\gamma-1}{\gamma}}\right] \tag{6}$$

It is possible to draw comparisons between the supplier maps for different turbochargers on the basis of a power absorption parameter,

$$\bar{W}_{\mathrm{t}} = \bar{\mathrm{m}}_{\mathrm{t}} \eta_{\mathrm{ts}} \left[1 - \pi_{\mathrm{t}}^{-\frac{\gamma(T_{0,\mathrm{in}})-1}{\gamma(T_{0,\mathrm{in}})}}\right] \tag{7}$$

where $\bar{m}_{\mathrm{t}} = (\dot{m}_{\mathrm{t}}\sqrt{c_{\mathrm{p}}(T_{0,\mathrm{in}}).T_{0,\mathrm{in}}})/(p_{0,\mathrm{in}}D_{\mathrm{wh}}^2)$ is the non-dimensional mass flow rate, computed from the reduced MFRs in the maps. When $\bar{W}_{\mathrm{t}}$ is plotted against the fully reduced turbine speed,

$$\bar{N}_{\mathrm{t}} = N.D_{\mathrm{wh}}/\sqrt{T_{0,\mathrm{in}}} \tag{8}$$

for the supplier maps, they all collapse onto axes of the same order of magnitude, with paths traced by the upper and lower limits of $\bar{W}_{\mathrm{t}}$ reflecting only on the surge and choke limits of the compressor used as the turbine loading device, and the limitations of the gas stand rig. This is shown for three of the reference maps in Figure 4. Of the selection of maps inspected, a suitable one was selected ('Ref. Map 3' in the figure), whose shape offered the most useful overlap with the wide map featured in this study. Broadly, the data of the wide map which remained inside (or close enough to) the $\bar{W}_{\mathrm{t}}$ boundaries of the reference map (and with < 2% deviation in reduced speeds), were retained and constituted the "supplier-width" (SW) map referred to herein. Consequently, the shape of the SW map and its lower flow limits were influenced by the definition of compressor surge adopted by the Ref. Map 3 supplier. A disadvantage of this data selection method is reduced resolution of $\bar{W}_{\mathrm{t}}$ with π_{t} at the highest powers.

The resulting SAE format flow and efficiency maps corresponding to these supplier width criteria are shown in Figure 5 and Figure 6. In order to test the effect of extrapolation of the maps in a progressive manner, some additional portion of the wide test map data needed to be reintroduced at each stage. An example of a slightly wider map is shown overlaid on the SW map in the same figures. This was obtained using scale factors (SF) applied to the $\bar{W}_{\mathrm{t}}$ ranges of the reference map (Figure 4), to specify the boundaries $\bar{W}_{\mathrm{t,SF}}^{\mathrm{test}}$ for extraction of data from the full wide map:

$$\bar{W}_{\mathrm{t,mid}}^{\mathrm{ref}} - \left(\frac{SF}{2}\right)\Delta\bar{W}_{\mathrm{t}}^{\mathrm{ref}} \leq \bar{W}_{\mathrm{t,SF}}^{\mathrm{test}} \leq \bar{W}_{\mathrm{t,mid}}^{\mathrm{ref}} + \left(\frac{SF}{2}\right)\Delta\bar{W}_{\mathrm{t}}^{\mathrm{ref}} \tag{9}$$

where $\bar{W}_{\mathrm{t,mid}}^{\mathrm{ref}}$ is the average of the limiting $\bar{W}_{\mathrm{t}}$ ranges in the reference map, and $\Delta\bar{W}_{\mathrm{t}}^{\mathrm{ref}}$ is the difference between the minimum and maximum values of $\bar{W}_{\mathrm{t}}$ in the reference map, for a given speed line.

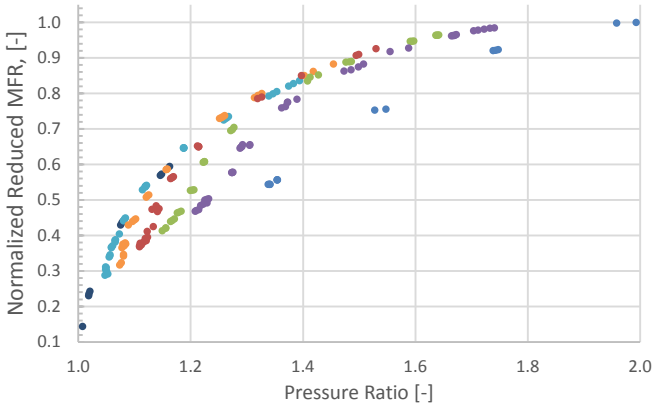

Figure 3. Full extent of test map flow capacity data in SAE format

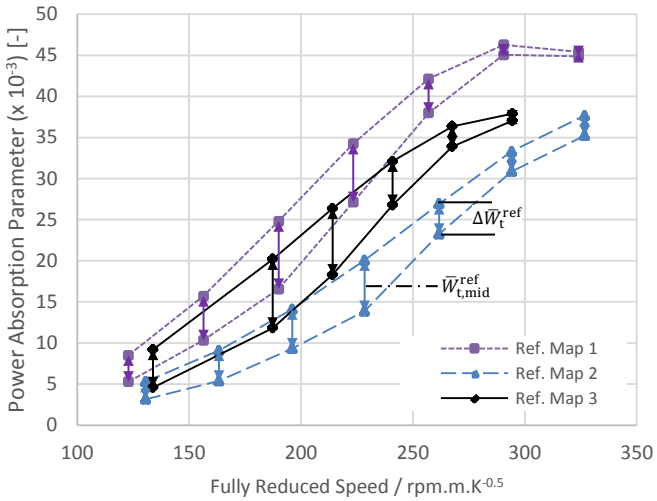

Figure 4. Widths of power absorption parameter across the range of fully reduced speeds contained in the data for three of the reference SAE maps

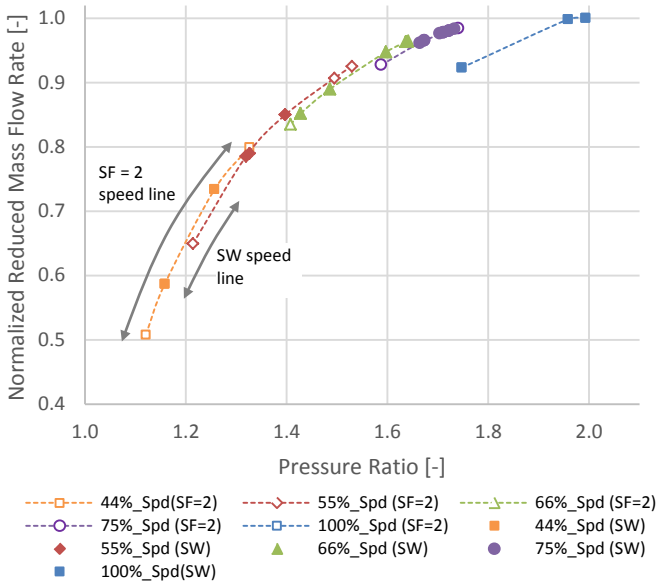

Figure 5. SAE flow capacity for supplier-width and scale factor 2 test maps

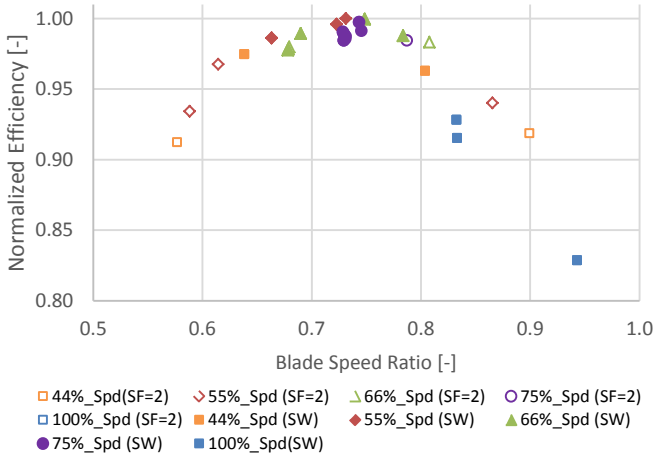

Figure 6. Efficiency vs BSR for supplier-width test map and test map enlarged by scale factor SF = 2

The scale factors applied were 1.5, 2, 3, 4, 5, 10 and 20, where the last value encompasses all the data, yielding the original wide map. Figure 7 shows the full extent of the original wide map data recast into $\bar{W}_t$ against $\bar{N}_t$, with the $\bar{W}_t$ boundaries for the SW map, and all seven test maps overlaid as dashed lines, indicating the specific data that were added to each speed line at each new scale factor. From here on the test cases of the study are referred to according to this scale factor – e.g. $SF = 2$ refers to a map or simulation for which the scale factor applied to the map width boundaries in Figure 7 was 2.

The map data in this study are normalized w.r.t. the maximum reduced speed in the full range of raw wide map data measured, leading to speed lines at 11%, 33%, 44%, 55%, 66%, 75% and 100% speed. As seen in Figure 7 the 11% and 33% speed lines lay outside of the typical supplier map $\bar{N}_t$ range, so these were also excluded from the first series of maps and simulations.

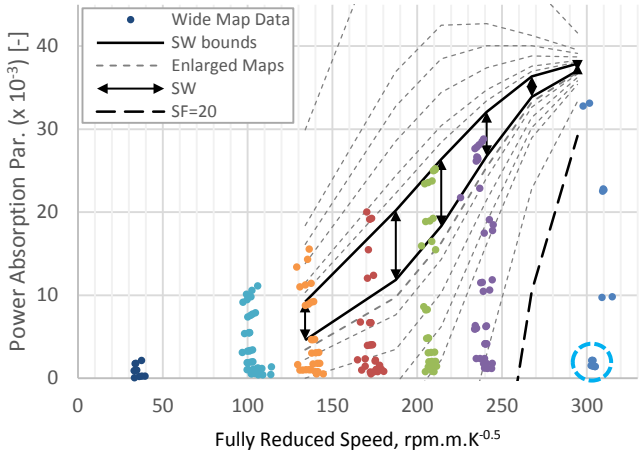

Figure 7. Power absorption parameter vs fully reduced speed for selected supplier map overlaid on measured wide map

It is important to note that due to the typical resolution of measured data in wide maps, new points were not necessarily captured in every speed line at every new SF both above and below the SW ranges. Thus some scale factors impacted certain speed lines more strongly than others. A second consequence of the map resolution is that the starting map widths differed significantly for each speed line (see Figure 5), potentially incurring varied amounts of extrapolation error for the SW case. Due to the inherent shape of the curves in Figure 7 it is obvious that additional points above the SW range of power absorption parameters will only be seen for the lowest two speed lines. Finally, the point at 100% speed with the lowest $\bar{W}_t$ (encircled) was retained for all the test maps despite being outside of all but the $SF = 20$ boundaries, and this was because the huge percentage difference in $\bar{N}_t$ for all other points on this line excluded them, making it otherwise impossible to form a proper speed line.

Parametric Study

This paper considers the two types of extrapolation applied to turbine maps – (1) the extension of existing speed lines to broader MFR and PR ranges, and (2) the construction of speed lines outside of the measured range of reduced speeds. For the first series of simulations, turbine maps were used with only the fully reduced speed ranges contained in the reference map, but with increasing coverage of wide map data on the speed lines (larger scale factors, and decreasing amounts of extrapolation). In the second series, the two additional speed lines characterized in the test map were added back in to the wide map, one by one, to create the case of minimal extrapolation.

Extrapolation Methodologies

In this work, two different extrapolation methodologies have been employed, in addition to that used in Dynasty™. The first, due to Payri et al. [11] is "physics-based", using thermodynamic and turbomachinery equations. It has been validated for several automotive turbocharger turbines, showing good agreement against measured wide data for both flow and efficiency. The second is a "black box" model consistent with low complexity, easily implementable numerical extrapolation adopted in control applications, where accuracy is less important. It is an adaptation of the method in [6]. A brief discourse on the methods is provided next.

Physics-Based Extrapolation

Using two simplifications relating the polytropic expansions in the stator and rotor, the theoretical turbine area of an equivalent nozzle [17], was recast [11] in a form requiring only basic turbine geometry:

$$A_{\text{eff}} = \frac{\mu_{\text{R}} A_{\text{R}} \cdot \sqrt{1 + k_{\text{a,1}} + \nu^2 \cdot \left[\left(\frac{D_2}{D_1}\right)^2 - 1\right]}}{\sqrt{1 + \left(\frac{\mu_{\text{R}}}{\mu_{\text{S}}}\right)^2 \left(\frac{A_{\text{R}}}{A_{\text{S}}}\right)^2 \frac{\left(k_{\text{a,2}} \cdot \frac{2\pi_{\text{t}}}{1+\pi_{\text{t}}}\right)^2}{\left(1 - \eta_{\text{ts}}\left(1 - \left(k_{\text{a,2}} \cdot \frac{2\pi_{\text{t}}}{1+\pi_{\text{t}}}\right)^{\frac{\gamma-1}{\gamma}}\right)\right)^2}}} \tag{10}$$

where D_1 and D_2 are the rotor entry and exit (r.m.s.) diameters, A_{S} and A_{R} the effective throat areas of the stator and rotor, multiplied by separate scale factors μ_{R} and μ_{S}, which are determined as part of the fitting process. The constant $k_1 = (C_0/C_S)^2 + (W_1/C_{\text{S}})^2$ is a function of the blade velocity triangles at rotor inlet, and the isentropic velocity C_{S}. Finally k_2 is a constant introduced to address errors caused by the thermodynamic assumptions. The constants are determined by fitting the model predictions to the real effective areas determined from the map data together with Equation (3), using a nonlinear least squares regression solver (the same is used to fit the measured efficiencies to the efficiency model outlined hereafter). For this study the 'nlinfit' function built into MATLAB R2015a, which uses a Levenberg-Marquardt algorithm [18], was adopted.

The total-to-static efficiency η_{ts} is obtained in three stages, starting with its definition in terms of gas specific enthalpies,

$$\eta_{\text{ts}} = \frac{h_{00} - h_{02}}{h_{00} - h_{2s}} \tag{11}$$

where stages '0', '1' and '2' correspond to the turbine volute inlet, the rotor inlet, and the rotor outlet respectively. Assuming a constant, average c_p the denominator is first expanded via the isentropic expansion equation. Then, equating Euler's Turbomachinery Equation, $\dot{W} = \dot{m}(U_1 C_{\theta 1} - U_2 C_{\theta 2})$, with the turbine power, $\dot{W}_{\text{t}} = \dot{m} c_{\text{p}}(T_{00} - T_{02})$, the numerator of Equation (11) is obtained and can be expressed in terms of rotor absolute and relative flow angles α_1, β_2, the blade tip speed, U_1, the nominal flow velocity C_0 (defined at the volute tongue) and flow radii r_1 and r_2. Finally, the isentropic velocity is related to C_0, via the continuity equation, assuming an ideal gas. The resulting equation for η_{ts},

$$\eta_{\text{ts}} = -k_{\text{e,1}} \nu^2 + k_{\text{e,2}} \left[1 - \frac{k_{\text{e,3}}}{\nu^2}\right]^{\frac{1}{\gamma-1}} \nu \tag{12}$$

is likewise fitted to the map efficiency data by tuning the constant $k_{\text{e,2}}$ defined $k_{\text{e,2}} = 2\, A_{\text{eff}}/A_0\, (\tan\alpha_1 + (r_2/r_1) \cdot \tan\beta_2)$. Note that $k_{\text{e,1}} = 2(r_2/r_1)^2$ and $k_{\text{e,3}} = U_1^2/2c_{\text{p}}\sqrt{T_{01}}$.

In the implementation of this model, the initial guesses for the efficiencies, across a fine resolution of PRs for each speed line, are substituted into the effective area model to obtain corresponding A_{eff} values. These are entered into Equation (12), to update the efficiencies. This cycle is repeated until acceptable convergence is achieved. The various extracts of wide map data are thus interpolated and extrapolated along the speed lines.

Black Box Model

The black box flow model starts with the same description of the MFR as a function of an effective area (Equation (3)). But instead of obtaining a physically based model for A_{eff}, its value is now simply fixed along a given speed line, for all pressure ratios. Since A_{eff} is no longer a function of the pressure ratio, the first unphysical implication of this model is that all the speed lines are forced through the $(\pi_{\text{t}} = 1, \dot{m} = 0)$ vertex. The use of constant effective areas also imposes restrictions on the shape of the flow curves, which do not conform to the data unless an allowance is made for π_t to appear as $\pi_{\text{t}}^{k_{\text{a,b}}}$ in Equation (3), where $k_{\text{a,b}}$ is a constant fitted to the map data:

$$\dot{m} = A_{\text{eff}} \sqrt{\gamma/R}\, \pi_{\text{t}}^{1/\gamma} \sqrt{\frac{2}{\gamma - 1} \cdot \left[1 - \left(\pi_{\text{t}}^{k_{\text{a,b}}}\right)^{\frac{\gamma-1}{\gamma}}\right]} \tag{13}$$

The constant $k_{\text{a,b}}$ can be thought of as an effective 'degree of reaction', reflecting the progressive nature of the expansion in a turbocharger turbine for which it is the *product* of the stator and rotor pressure ratios, p_{00}/p_1 and p_1/p_2 that determines the overall PR. This enables much greater values of π_{t} (of order double) than those observed in a simple restriction for the same mass flow.

The black box efficiency model fits the entire set of efficiency map data to a single quadratic in ν:

$$\eta_{\text{ts}} = \eta_{\text{ts}}^{\max}\left(1 - k_{\text{e,b}}\left(\nu - \nu(\eta_{\text{ts}}^{\max})\right)^2\right) \tag{14}$$

where $\eta_{\text{ts}}^{\max}$ is the representative maximum efficiency in the map, and $\nu(\eta_{\text{ts}}^{\max})$ the BSR at which it occurs, and $k_{\text{a,b}}$ is a fitting constant of the model. The black box flow and efficiency models are not interdependent and no convergence routine is required to extrapolate the map data. For maps of $SF > 3$ the flow model R^2 values were unacceptably low (< 0.95) for the 44% and 55% speed lines (which, as it will be seen, had the greatest impact on the transients of this study); therefore no black box maps were considered for $SF > 2$.

Preparation of Maps

The test maps submitted to the engine simulation comprised of the interpolated regions and extrapolated regions:

1. Interpolated regions ('a' in Figure 8) of each speed line were the converged outputs of the physics-based model, conforming to shape of the original points ("map data" in Figure 8) at each SF
2. Data in the extrapolated regions ('b' and 'c' in Figure 8), either:
    a. Extrapolated points from the physics-based model (continuation of the curves in (1)); or
    b. Extrapolated points from the black box model; or
    c. Extrapolated points generated by the proprietary software

All speed lines were created from the same PR array. The spacing between data in Ref. Map 3 was seen to increase with PR, and this was replicated in the array. This effect may be due to the specific method used to traverse along a speed line on the gas stand. The final map submitted to the engine simulation was the result of internal processing by Dynasty™, which incurred some unquantified interpolation error. Pressure ratios above 2.1 (region 'd' in Figure 8) were not modelled since the transients were known to finish with the turbine not far exceeding this value. Except when the 11% and 33% speed lines were reintroduced, data for speeds below 44% were generated purely by Dynasty™. Finally, no choking routine was used in conjunction with either the physics-based or the black box extrapolations, so the reduced mass flows in the physics-based and black box maps is unphysical beyond the choking pressure ratio $\pi_{t,c}$. This did not affect the simulation results as the maximum turbine pressure ratio for all transient test cases was sufficiently below $\pi_{t,c}$.

When the turbine map data are measured on a cold flow rig such as at Imperial College, heat transfers and mechanical losses are not part of the turbine efficiency as in typical supplier maps. This affects the resulting model fit, however, no mechanical loss or heat transfer models were implemented in the engine model so that these phenomena were comprehensively ignored throughout this work.

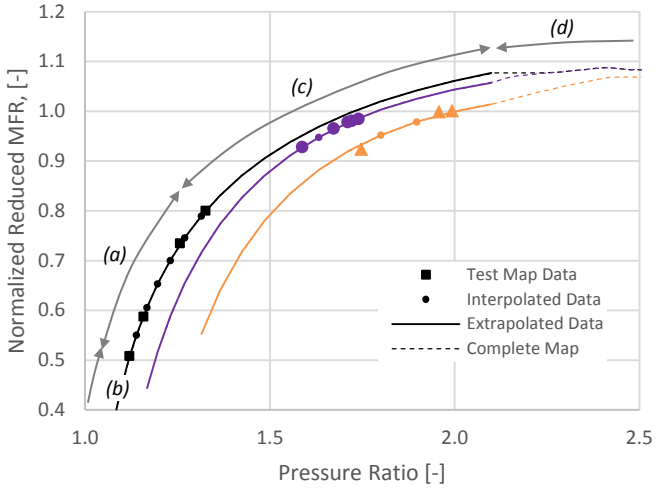

Figure 8. Extrapolated test map constituents

Engine Transient Simulation

Engine design teams typically have a range of transient cycles used to assess the suitability of engine-turbocharger match, quantify the impact of design changes, and qualify engines for service. These cycles are frequently designed to replicate real-life transients (which may or may not have been sampled previously) though this is not always the case. The torque/speed control will depend on the way in which the power generated by the prime mover is transmitted to the machine's functional head (e.g. a drive shaft, or a scoop). First a general overview of engine transients is given, followed by specific details of the TCS and CSLA and the Dynasty™ model setup.

Engine Transients

Similar to the analysis of a transient acceleration given by Rakopoulos and Giakoumis [19] a transient cycle can be divided into three phases. These are illustrated below in Figure 9 for a constant speed transient. In the first phase, a significant amount of fuel can immediately be injected in the cylinder since excess air is present. For our example case, this increases the torque from minimal starting load to 63% of the full load torque. During this phase the fueling increases to the value dictated by the "boost limited fueling".

During the second phase the fuel rate is limited by the boost control strategy until the maximum fuel rate is reached. This is shown in the second row of Figure 9 where the fueling rate is plotted. During this phase, the air-to-fuel ratio is much lower than the steady state value and the TIT significantly exceeds the steady state value. For this example, at the end of the second phase, the fueling reaches its final value but the torque is still 10% lower than the steady state value. This is because the boost has only increased to 50% and the BSFC is still well below the steady state value. As Rakopoulous mentions [19], the fueling is limited during this phase, mainly due to smoke emissions. However, with the presence of after-treatment equipment, the fueling level can sometimes be increased during transients.

Finally, during Phase 3 of the transient, the boost increases to its steady state value and the engine gradually approaches full torque operation. The TIT decreases during this portion of the cycle. Rakopoulos and Giakoumis include a segment of constant fueling during a turbo lag period. For this simulation, the increase in fueling level was relatively constant for the entire boost-limited portion.

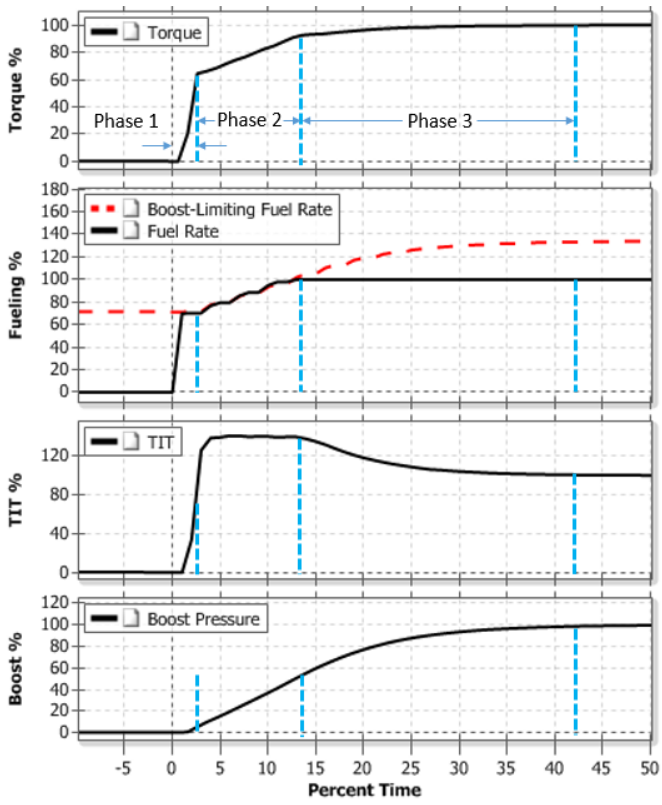

Figure 9. C175 constant speed transient. The scale was normalized at the start and end of the cycles to show the relative changes during the transient.

Torque Converter Stall (TCS)

The first transient referred to in this study is the torque converter stall. This simulates the engine with the crankshaft linked to a torque converter, a type of fluid dynamic coupling which is widespread in automotive and heavy duty vehicular drivelines for power transmission. This test would be conducted for an engine installed in the machine for which it was designed (in this case a mining truck). The transient cycle begins with the engine at low idle operation; then the engine speed and torque increase to full load along the curve dictated by the torque converter in a stalled condition – at which the torque converter input absorbs the maximum torque for a given

rotational speed. An example is shown in Figure 10. The transient response time may be evaluated based on such criteria as the time to clear the smoke map, the time taken to intersect the engine's lug curve, or time to a specified engine speed. A common definition in terms of speed is the duration between a measure of the start of the transient (e.g., the time when the throttle position reaches 50%) and when the engine speed reaches 90% of the stall speed (normalized speed '1' in Figure 10). The latter is the definition used in this work.

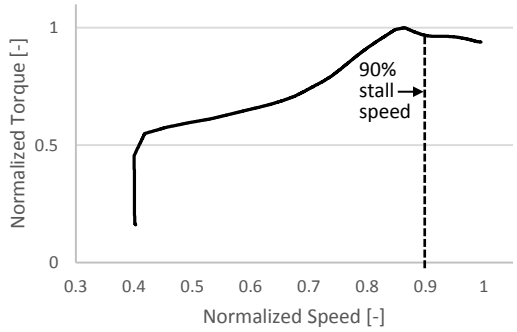

Figure 10. Example of a TCS torque-speed curve

Constant Speed Load Acceptance (CSLA)

The second type of transient examined was the constant speed load acceptance. In this case the cycle runs from low load to full load with the engine speed held constant. The CSLA characterizes the load an engine is capable of accepting instantly at a given speed. This type of transient is performed with the engine coupled to a dynamometer, which is programmed to adjust the applied resistance continuously as the engine sweeps through operating states, restraining the speed from changing. For the CSLA the response time is defined in terms of engine torque since the speed is constant. A common criterion, used here, is the time to reach 85% of the maximum torque. The CSLA can be run at different engine speeds; the higher the engine speed, the shorter the time to 85% torque. Since the engine torque fluctuates substantially through each engine cycle, a previous cycle average (PCA) signal was used to evaluate TR times. The signal was first smoothed so that the precision could be much better than a cycle period. A consequence of using PCA signals is that the absolute value of TR time is increased by around half a cycle period, but since the aim is to investigate the relative *difference* in TR times, this is of little consequence. A greater impact due to extrapolation was expected to be observed in the TCS simulations, since in the CSLA the torque very rapidly moves to a point close to its final value, seemingly leaving less time for the turbo lag to have an influence.

1D Engine Simulation and Platform

As mentioned, the transient engine simulations were conducted using the Caterpillar Inc. Dynasty™ program [21–23]. This program thermodynamically models various elements such as the combustion chambers, valve elements, ducts and turbochargers in order to simulate the engine performance. In addition, Dynasty™ not only simulates the engine operation, but also has the capacity to model the drive train and other components to simulate the entire machine [24,25]. For this study, a C175 16 cylinder tier 2 engine model was selected. The engine is shown in Figure 11. It uses 4 single stage turbochargers and a common rail fuel system and is configured for operation in the Caterpillar 793F mining truck. The rated horsepower is 1748 kW at 1750 rpm. The bore and stroke are 175 mm and 220 mm respectively and the piston displacement is 85 liters. The engine model was matched to both steady state and transient engine data. It should be noted that, for this study, the turbocharger was altered from the production model, to accommodate the measured test turbine map. Specifically, the area scale factor for turbine maps (a scale factor applied to the MFR reading from the map) was set to a value less than 1, and the turbine rotational inertia was raised to bring the engine transient predictions back in line with measured data. The single entry turbine negated any partial admission or cross-talk models. The compressor is a commercially available Honeywell model with a 92mm diameter wheel.

Figure 11. Caterpillar C175-16 engine (left) used in the Caterpillar 793 Mining Truck (right)

Results and Discussion

This section presents the most important outcomes of the study, alongside discussions on their likely cause and implications – starting with the most notable percentage effects on transient response, then moving to a transient and extrapolation method-specific analysis.

Effect of map widening

The following figures chart the percentage change in the transient response time prediction, relative to the time simulated for the SW case – for progressive reduction of the extrapolated map regions, and for each transient, for the three extrapolation routines. Note that no simulations were carried out for the physics-based $SF = 3$ map since it emerged that this map contained an anomaly in efficiency.

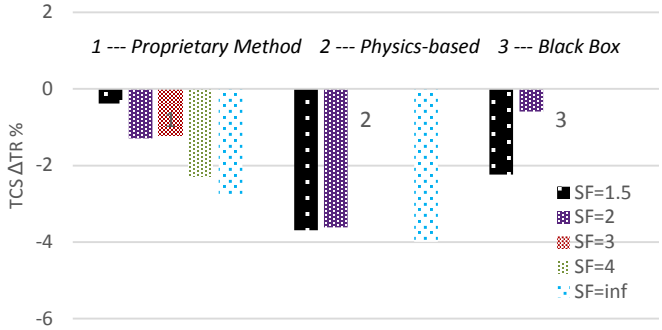

Figure 12. TCS map widening – effect on transient response

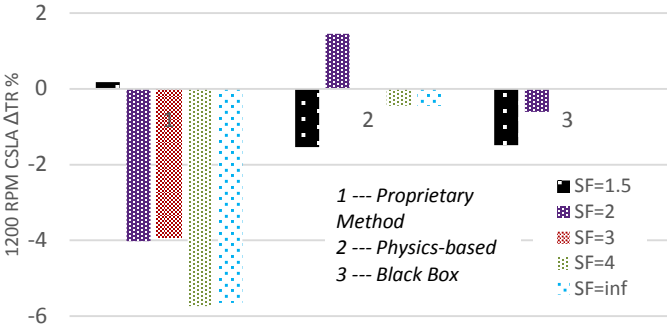

Figure 13. 1200 RPM CSLA map widening – effect on transient response

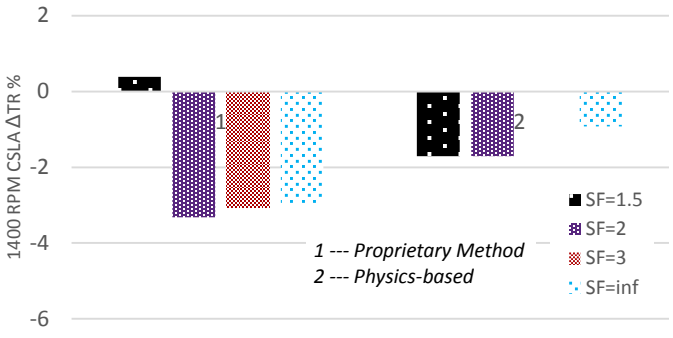

Figure 14. 1400 RPM CSLA map widening – effect on transient response

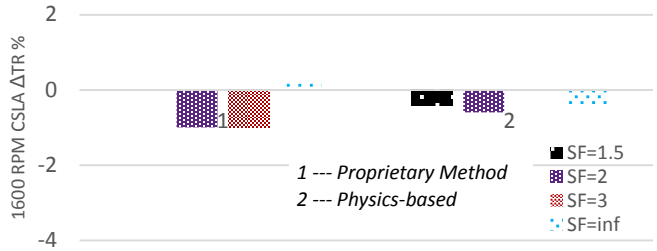

Figure 15. 1600 RPM CSLA map widening – effect on transient response

It is seen that for almost every map width, transient and extrapolation technique, the effect of reducing extrapolation was a faster transient response. Since the absolute TR times predicted using the SW maps were already fast compared to the engine data, map widening has revealed that the original transient prediction was even worse than originally suspected. Except for the TCS and the 1200 RPM CSLA proprietary cases, the percentage effect of extrapolation on the TR times was apparently uncorrelated with the exact amount of extrapolation introduced. It also emerges that for all but the two cases singled out above, the greatest effect on transient response is already seen within the range of maps $SF \leq 2$.

The most strongly affected transients were the TCS and the 1200 RPM CSLA. The TCS saw maximum changes of -2.8% ($SF = 20$), -3.9% ($SF = 1.5$) and -2.2% ($SF = 1.5$) for the proprietary, physics-based and black box extrapolations respectively. Similarly the 1200 RPM CSLA saw maximum changes of -5.7% ($SF = 4$), -1.5% ($SF = 1.5$) and -1.5% ($SF = 1.5$) for the three methods.

Proprietary extrapolation results – CSLAs

The greatest deviations in the simulated TR times from the proprietary maps were for the 1200 RPM CSLA. Indeed, as Figure 13 through Figure 15 show, the CSLA transients showed a steady decline in the maximum effect on TR time for each new (higher) engine speed. Figure 16 shows the PCA turbine efficiency (normalized w.r.t. the maximum efficiency in the wide map) for the 1200 RPM and 1600 RPM CSLAs, overlaid on the SW and $SF = 20$ maps used to generate them. Figure 17 shows the normalized reduced speeds with normalized time. In contrast with the TCS, the CSLA transients all remain within the SW map N_{red} ranges. One immediate artefact is that in the first part of the cycle, N_{red} decreases with the PR, due to the very high ramp in TIT over the first few engine cycles. Considering that the spaces between PCA points represent one engine cycle in the time domain (and the engine cycle times are constant for the CSLA) the time period of this initial decrease in N_{red} is small (< 3 engine cycles) compared to the remainder of the transient. After the minimum N_{red}, the transients "double back" on themselves for 1-2 engine cycles, before settling to an increasing function of the PR.

As mentioned earlier, the smoke-limited fuel rate at the target torque is higher than at engine idle where the transient starts, so a delta in boost is needed to allow the fuel flow to increase and to complete the transient. Keeping in mind from Figure 9 that the linear phase of fuel flow with boost occupies most of the transient up to 85% torque, it then seems sensible that variations in boost pressure should explain the difference in TR times. The percentage difference in boost pressure for the $SF = 20$ case relative to the SW case is shown against normalized time for the three CSLAs in Figure 18. The final values (8.8%, 4.0% and -1.1%) correlate well with the corresponding differences in TR time (-5.7%, -2.9% and 0.2% respectively). The compressor efficiencies and turbine flows during these transients did not differ between $SF = 20$ and SW. Thus comparing the $SF = 20$ and SW efficiencies in Figure 16, the departure of the $SF = 20$ boost traces from SW is clearly dictated by the relative efficiencies through the transient. The specific regions of interest on each of the speed lines, at the relevant parts of the transients, are indicated by the thicker line portions in Figure 16. The 1600 RPM CSLA seems to have been more affected by the 75% speed line for which $\eta_t^{SW} > \eta_t^{SF=20}$ for all PRs. This is reflected in the boost pressure traces for which the percentage difference of $SF = 20$ relative to SW is initially negative. The impact on TR times from map widening was consequentially small for the 1600 RPM CSLA.

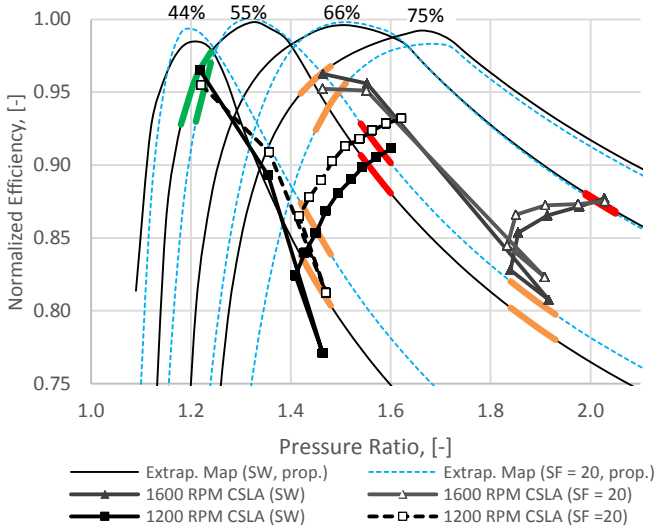

Figure 16. 1200 RPM and 1600 RPM CSLA transients PCA normalized efficiency variation with pressure ratio – SW and SF = 20 map cases

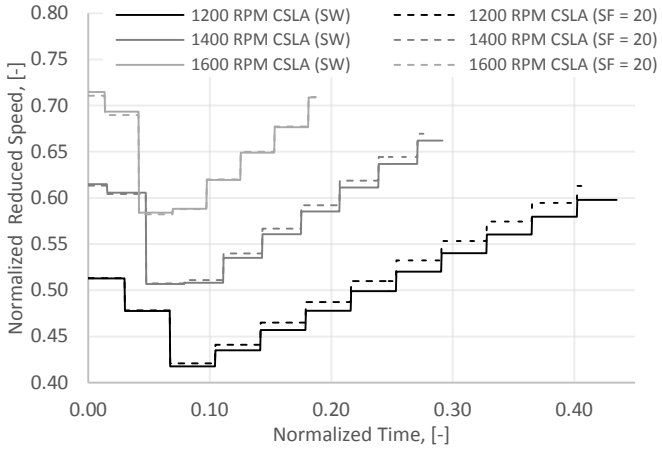

Figure 17. CSLA transients PCA normalized reduced speed variation with normalized time for the SW and SF = 20 map width cases

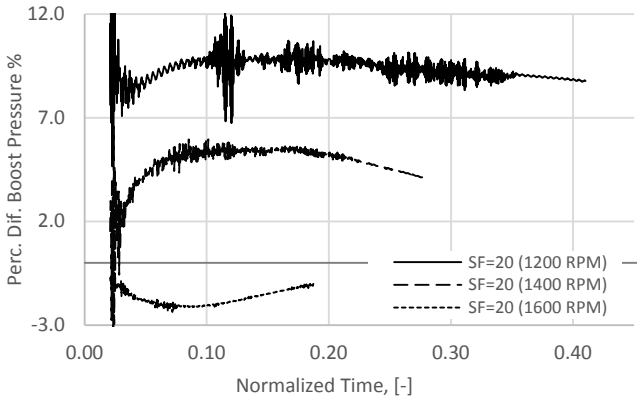

Figure 18. CSLA transients %-age difference in boost, SF = 20 relative to SW

When comparing boost pressures it is important to recognize that transient response is a *system* effect and depends on the net outcome of multiple interactions and variations. It is therefore useful to relate final differences in boost pressure to some cumulative variable – in this case the cumulative turbine energy supply. To compare transients on this basis a relative divergence parameter (Y^{SF}) is defined:

$$Y^{SF} = \frac{E_t^{SF} - E_t^{SF_{ref}}}{E_t^{SF_{ref}}} \times 100\% \qquad (15)$$

where E_t is the cumulative turbine energy supplied by normalized time t (evaluated as the product of turbine torque and rotational speed), SF is the map of interest, and SF_{ref} is the map against which the comparison is made (SW for map width tests, $SF = 20$ for speed line addition tests). Figure 19 shows this parameter.

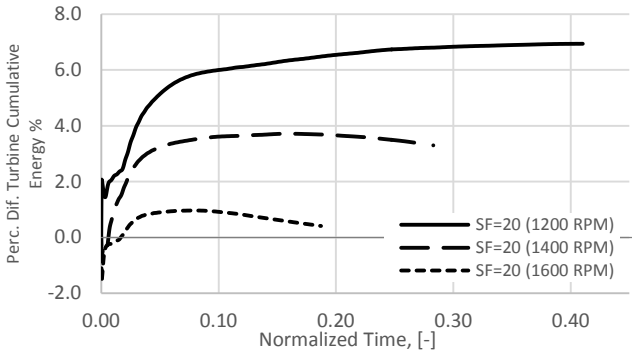

Figure 19. CSLA transients - deviation of cumulative turbine energy supply for SF = 20 cases relative to SW cases

The variation is similar to the boost pressure, but does not account for the compressor efficiency (cumulative compressor absorbed power could not be obtained due to a limitation of the simulation). Through-transient variation of *Y* reveals the extent of the extrapolation error affecting the simulation. *Y* may attain very high values early on without significantly impacting the engine transient, since while the turbocharger speed is low, the influence of the turbocharger on engine performance is small. However the large *Y*-values indicate a substantial difference in the total increase in turbocharger speed that took place during these early periods, and as a result the *Y* may never return to zero even as turbocharger power increases, leading to a net offset at the end of the transient. Thus the final *Y*-values are representative of the holistic effect of extrapolation error on transient response, and exhibit some correlation with percentage difference in TR time. Here the final Y^{20} values of 6.9%, 3.3%, and 0.4% correspond to percentage differences of -5.7%, -2.9% and 0.4% in TR time relative to SW, for the 1200, 1400 and 1600 RPM transients respectively. Y^{20} for the 1400 and 1600 RPM transients peaked at lower values due to smaller differences in η_t^{SW} and η_t^{20} experienced in the maps (the $SF = 20$ 1600 RPM started at a slightly lower speed, as the increased map width also impacted initial conditions).

Black-box extrapolation method results – TCS

shows the displacement of efficiency curves due to widening of the map from SW to $SF = 1.5$ and $SF = 2$ respectively, highlighting specific data points that engendered these displacements.

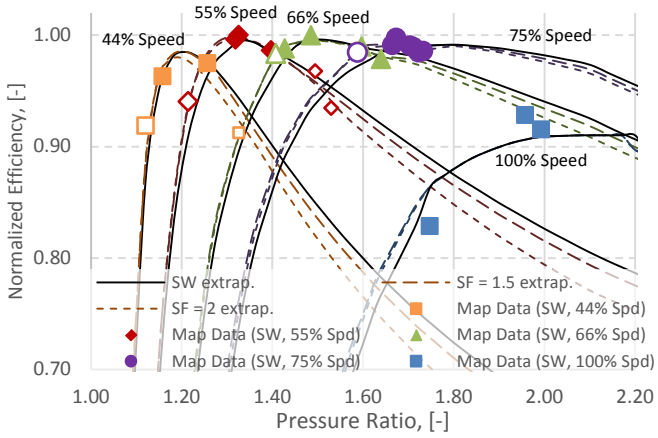

Figure 20. Widening of map data – effect on efficiency extrapolation (black box extrapolation); open markers show SF = 1.5, small open markers SF = 2

The normalized efficiencies for the TCS transients corresponding to these three starting maps are displayed in Figure 21 (against PR), while their variation with normalized time is shown in Figure 22.

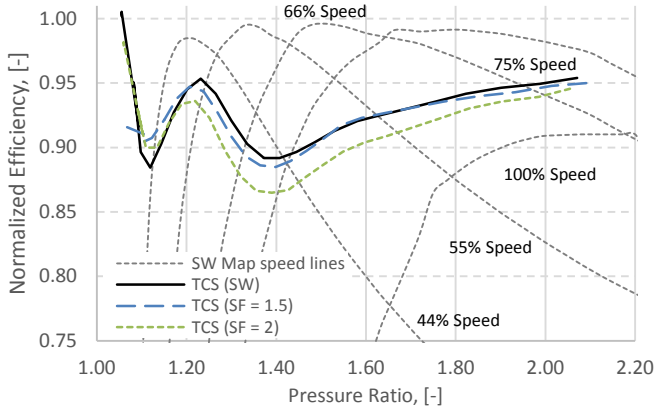

Figure 21. PCA TCS black box transients – SW, SF=1.5 and SF=2

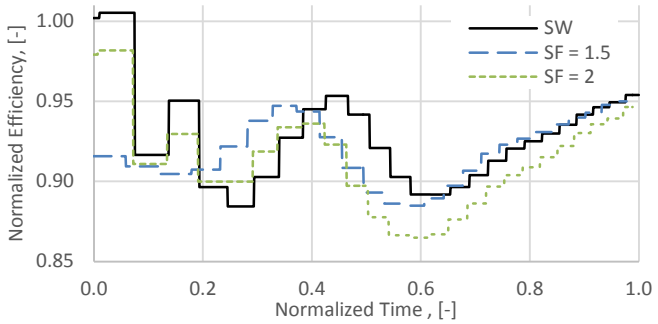

Figure 22. TCS transients PCA normalized efficiency with normalized time

During these transients, the operating point starts outside of the region of the map data, only crossing the first speed line (44% speed) at a normalized time of around 0.8. This means that the speed line of greatest impact was the 44% line. Following intersection of this speed line η_t then continues to rise, steadily, passing through the 55% and 66% speed lines, and ending at the 75% speed line. It should be noted that the starting reduced speeds are different for the three cases ($SF = 1.5$ and $SF = 2$ start 4.6% and 2.5% faster than SW respectively, giving a 0.69% and 0.35% 'head start' in terms of turbocharger rotational energy). This combined with the favorable η_c (see Figure 23) over $0 < t < 0.28$ caused an early rise in $Y^{1.5}$ and Y^2 which are shown in Figure 24. This offset was heightened between $0.15 < t < 0.3$ where $\eta_t^{1.5,2} > \eta_t^{SW}$, and $Y^{1.5}$ and Y^2 peaked at 31.1% and 12.5% respectively, before the gap was closed again over $0.3 < t < 1$ where $\eta_t^{SW} > \eta_t^{1.5,2}$. The final $Y^{1.5}$ and Y^2 (at 12.0% and 2.5% resp.) again correlate somewhat with the relative deviation in TR times (-2.2% and -0.6%) although the scaling is different, possibly because Y does not account for compressor efficiency.

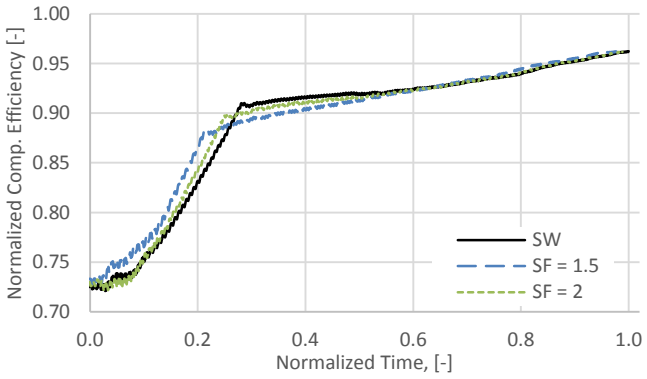

Figure 23. TCS transients compressor efficiency (normalized w.r.t. the maximum η_c occurring in the compressor map) with normalized time

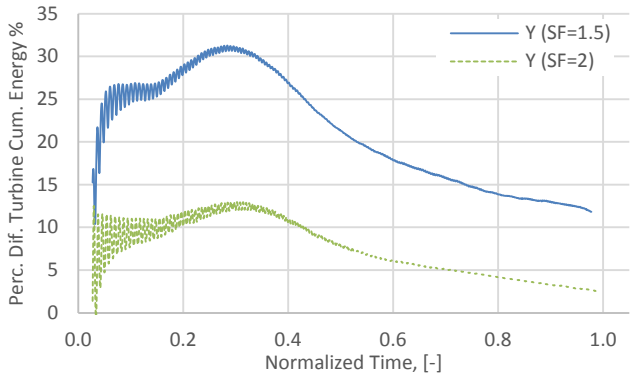

Figure 24. Percentage difference in cumulative turbine energy supply with normalized time for SF=1.5 and SF=2 relative to SW

The peak engine torque occurs just before the 90% crankshaft speed threshold is reached, and it is interesting to see in Figure 25 that the peak torque for the SF=1.5 and SF=2 cases was around 4.4% and 1.2% higher respectively, than for the SW case, indicating these transients reached a different location on the engine's lug curve.

Effect of addition of speed lines – TCS Response

The second series of simulations carried out in this study consisted in studying the effect of adding speed lines for speeds below the fully reduced speeds range in typical supplier-width maps. The addition of one speed line (33%) caused a 3.1% increase in the TR time compared to the $SF = 20$ case, whilst the addition of the second (11%) line resulted in a 4.2% increase. Figure 26 shows the variation of normalized η_t for the TCS transients, corresponding to the three cases $SF = 20$, $SF = 20$ (+1 spd) and $SF = 20$ (All spds). The normalized efficiencies with normalized time are shown in Figure 27. The TCS transients reach the 44% speed line at a normalized time of around 0.52, at which time $\pi_t \approx 1.4$, so the impact on efficiencies is, as expected, only seen for pressure ratios below this value. The impact is substantial, with peak variations of 13.8% and 15.8% respectively, relative to the $SF = 20$ case.

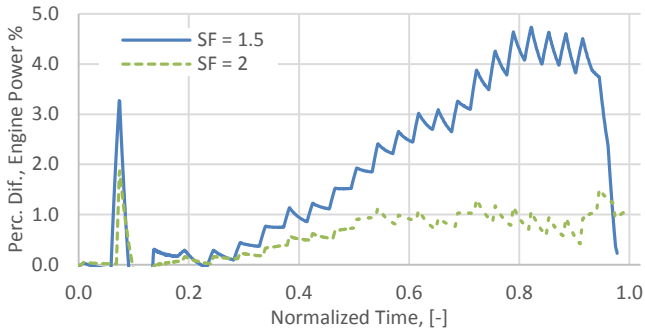

Figure 25. TCS transient percentage engine power deviation of SF=1.5 and SF=2 cases relative to SW case

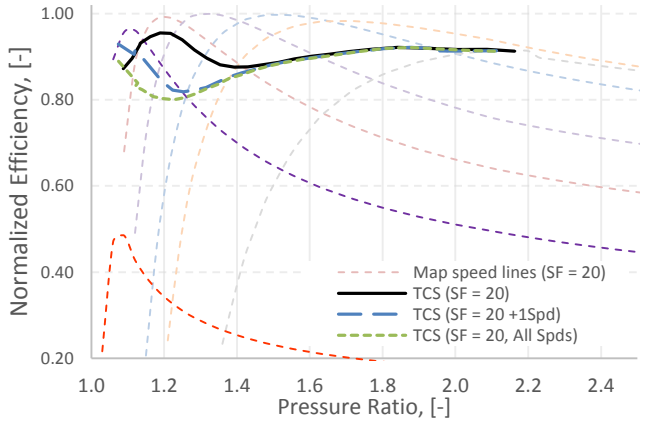

Figure 26. PCA TCS transients normalized efficiency with pressure ratio, showing all seven speed lines generated by the physics-based model

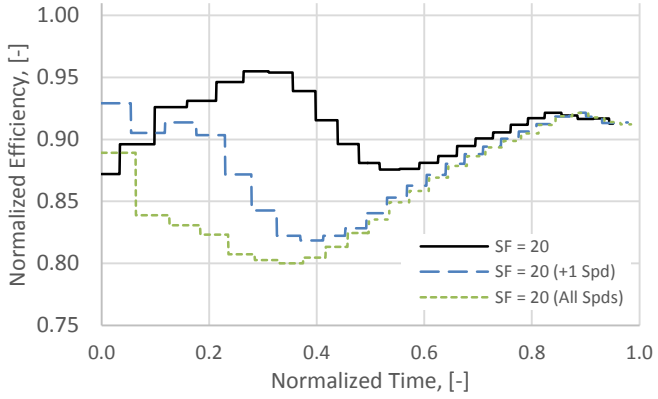

Figure 27. TCS transients PCA normalized η_t with normalized time for *SF* = 20, *SF* = 20 (+ 1Spd) and *SF* = 20 (All Spds) with physics-based extrapolation

$Y^{20\ (+1\ \mathrm{Spd})}$ and $Y^{20\ (\mathrm{All\ Spds})}$ are shown in Figure 29. Here the lower estimation of η_t for $N_{red} < 44\%$ by Dynasty™ causes an early offset, which peaks at around $t \approx 0.4$ and never recovers as the map widening effect of is not present. In Figure 29 the engine power difference is shown with normalized time. Even after $t = 0.52$ the deterioration of engine performance compared to $SF = 20$ continued – up to $t \approx 0.91$ when the engine's lug curve was reached and a peak torque observed. The longer transients are also associated with greater fuel consumption, at +1.8% and +2.6% respectively.

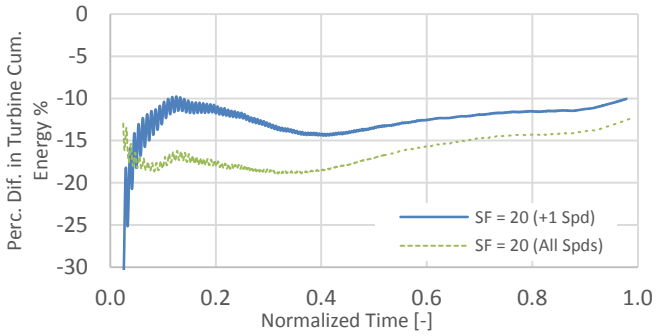

Figure 28. Percentage difference in cumulative turbine energy supply with normalized time for SF = 20 (+1 Spd) and SF = 20 (All Spds) relative to SW

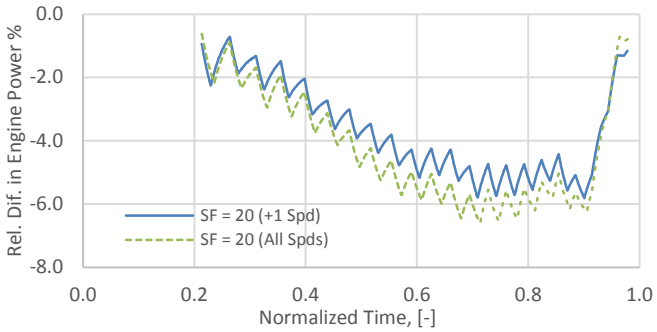

Figure 29. TCS transients percentage deviation in engine crankshaft power for the SF = 20 (+ 1 Spd) and SF = 20 (All Spds) cases relative to the SF = 20 case (showing only $t > 0.2$ due to the early oscillations)

Comparison of extrapolation models

The third and final feature of this study was the evaluation of how the extrapolation models used to produce the maps differed in their predictions for progressive map widening, and the consequences on simulated TR times. A summary of the percentage disagreements in TR times is provided in Figure 30, Figure 31 and Figure 32 for the TCS, 1200 and 1400 RPM CSLAs (the 1600 RPM CSLA results are omitted since they were all < 1%). A first observation is that whilst the results for the proprietary and physics-based methods seem to converge on each other somewhat as the SF increases, those for the black box method are seen to *diverge* from the former. This could be indicative of a lacking ability of the black box model to fully represent the behavior of the turbine over the full range of pressure ratios, owing to the absence of inbuilt physical principles.

To understand the reason for the discrepancies, the 1200 RPM CSLA and TCS transients have been analyzed for the first two stages, $SF = 1.5$ and $SF = 2$, as well as for the SW case. The general expectation was that the disagreement between the models should reduce as the coverage of measured data in the maps increased. There ought therefore to be smaller disparities between the TR times for each new SF. Contrarily, the most severe disagreement between TR predictions for the 1200 RPM CSLA occurred at $SF = 1.5$, where the percentage differences in TR times for the proprietary and black box methods relative to the physics-based method were +7.5% and +3.1% respectively. The physics-based and proprietary models actually grew further apart moving from SW to $SF = 1.5$.

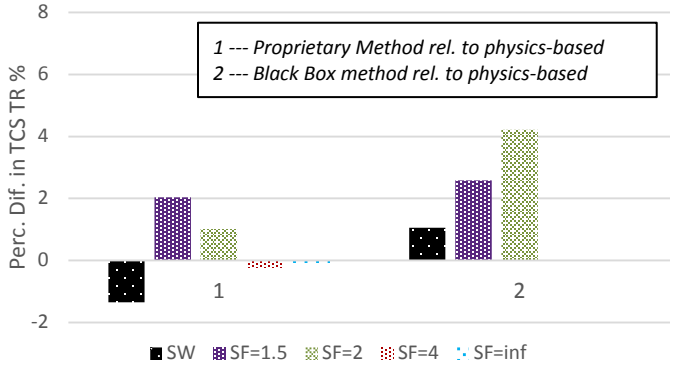

Figure 30. Percentage difference in TCS TR time predictions based for proprietary and black box extrapolations relative to the physics-based method

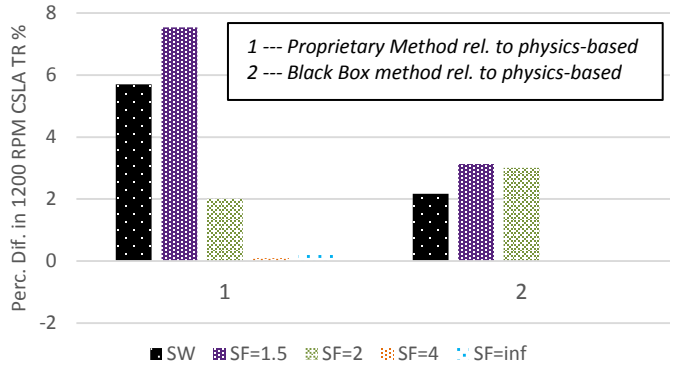

Figure 31. Percentage difference in 1200 RPM CSLA TR time predictions for proprietary and black box extrapolations, relative to the physics-based method

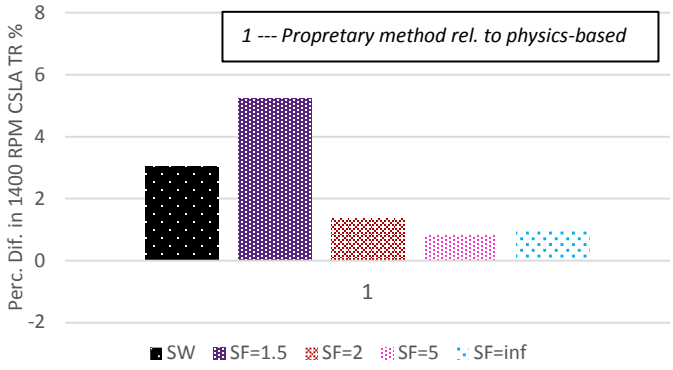

Figure 32. Percentage difference in 1400 RPM CSLA TR time predictions for proprietary and black box extrapolations, relative to the physics-based method

The range of reduced speeds covered in the map by the CSLA transients is smaller than for the TCS transients (around 18.0%, 15.4% and 12.5% for the 1200 RPM, 1400 RPM and 1600 RPM respectively compared to 47.6%). The TCS transients for the SW and $SF = 1.5$ cases are shown for the three extrapolation models, together with the corresponding 44%, 55% and 66% speed lines, and

the starting map data from which the maps were extrapolated, in Figure 33 and Figure 34. At SW, for $1.09 \leq PR \leq 1.15$ the proprietary model gave an elevated average η_t prediction of 4.9% and 10.7% relative to the physics-based and black box models respectively. The addition of the point at $PR = 1.12$ on the 44% speed line in the $SF = 1.5$ map has brought the three models closer together for this band of PRs, whilst moving them apart to the right of the inflexion. As a consequence the difference in TR predictions for the proprietary and black box extrapolations relative to the physics-based prediction, *increased* to +2.0% and +2.6% respectively.

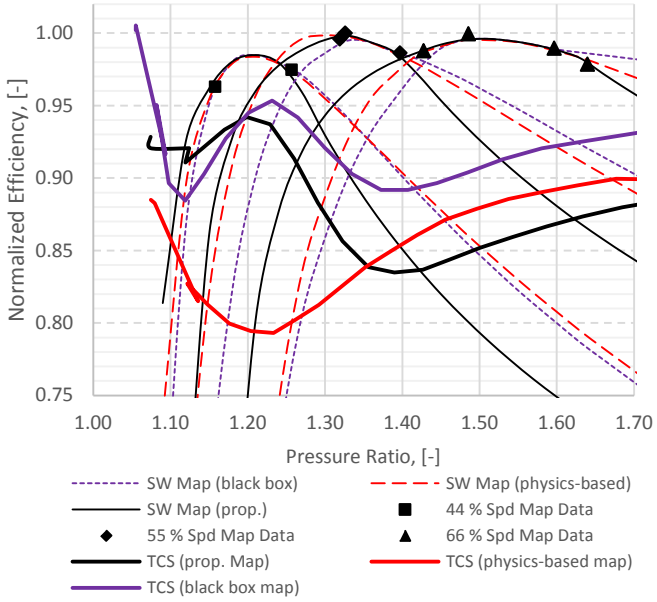

Figure 33. Original map data, extrapolated maps produced by the physics-based, black box and proprietary models, and the PCA TCS transients for the SW map case

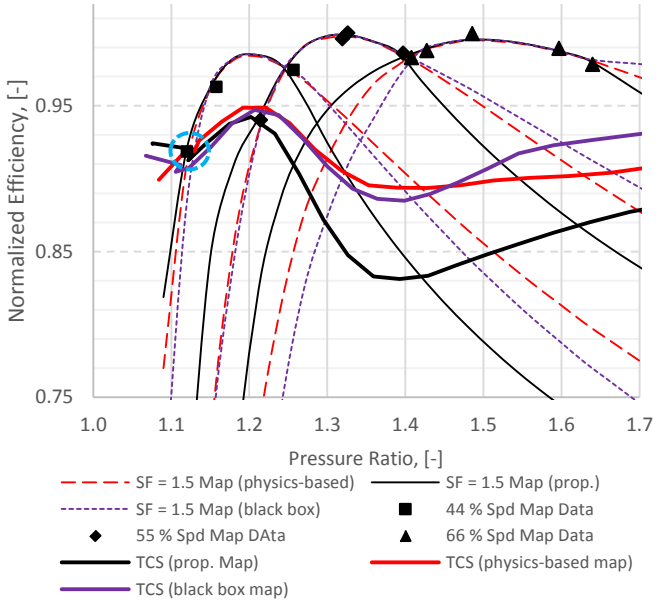

Figure 34. Original map data, extrapolated maps produced by the physics-based, black box and proprietary models, and the PCA TCS transients for the SF = 1.5 case

General discussion

A key message from these results is that the variation in transient response prediction due to map extrapolation error is not only due to different initial conditions (turbine and compressor reduced speed) due to a different steady state turbine and compressor match. A 5.7% decrease in TR prediction was observed for the 1200 RPM CSLA for the $SF = 20$ case compared to the SW case, whilst the starting reduced speeds for these two cases were identical. Extrapolation error can therefore be responsible for a significant amount of through-transient deviation of engine power in addition to the starting offset.

Comparing Figure 19 and for the deviations of the proprietary CSLA and black box TCS cumulative turbine energy respectively, it is evident that simply comparing the predicted and measured engine TR times does not tell the full extent of the error in transient simulation due to extrapolation. The TCS spent a large portion of the transient at $PR < 1.2$, under heavy influence of the 44% speed line left of its inflexion point where $\eta_t^{1.5}$, η_t^2 and η_t^{SW} were in reverse orientation compared to the right of the inflexion. Some of the early deviation in the TCS simulation was counteracted in the later stages due to this reversal, disguising the maximum error and causing the TCS to appear less affected than the CSLA. This disguise could have been even more pronounced had the effect of speed line addition also been present, potentially cancelling the error entirely.

Of particular interest is that the black box method showed the lowest impact on TR times due to map widening, despite its minimal complexity and lack of physical principles. In fact, beyond $SF = 2$ the black box model was no longer able to produce an adequate fit to the data. Thus it is likely that whilst the physics-based and proprietary models fluctuated with increasing SF as they gradually converged on the true turbine steady-state behavior, the black box model did not respond in the same way and its efficiency curves did not likewise converge with the reintroduction of measured data. Hence the lower percentage difference in predicted black box TR times should not be viewed as an indication of better accuracy.

Finally, it must be emphasized that there were fundamental differences in the way that each extrapolation model responded to additional wide map data. The black box model inflexion points moved to the left whilst η_t dropped to their right. For the proprietary model the inflexion points were relatively unaffected but η_t dropped substantially to their left, and increased to their right. For the physics-based model η_t fluctuated, and finished fairly close to the SW curve (implying a higher level of accuracy). For this reason, for an arbitrary engine transient event, in order to anticipate the presence of error in simulation due to map extrapolation, it is necessary to have some understanding of the general $N_{red} - \pi_t$ trajectory through the map.

Conclusions

The sensitivity of transient response prediction of a turbocharged diesel engine to extrapolation of turbine maps used in a predictive 1D engine model has been evaluated. Starting with a wide map measured on a cold-flow turbine dynamometer, modified maps of various widths and with additional speed lines were produced and used in the engine simulation. The maximum impact on the predicted torque converter stall transient response time due to map widening was 3.7%, while those for 1200, 1400 and 1600 RPM constant speed transients were 5.7%. 3.3% and 1.0%. These differences were caused by a 4.5% efficiency deviation on the 44% speed line. Three extrapolation models were tested: physics-based, black box, and the proprietary method used in the Caterpillar Inc. Dynasty™ program. The maximum disagreement in transient response predictions based on maps generated by these methods was 7.5%. The black box

model, which is not based on physical principles, was not able to produce a good fit to the wide map data beyond map widths of twice a typical supplier map width. The map widening caused an almost unanimous decrease in transient response time, which further increased the error between the simulation and the measured engine transient data compared to using the original supplier map.

Adding entire speed lines to a map at the low speed end increased the transient response time. Conversely, increasing map width by reintroducing measured data reduced the simulated transient response time. The 44% speed line was responsible for the greatest differences in transient response prediction. Its widening had different effects for each extrapolation model. For the physics-based model, it increased efficiencies to the left of the inflexion point and decreased them to the right. For the proprietary model, the opposite effect was seen. For transients passing only through regions to the right of inflexion points the impact is greater than for those starting at very low pressure ratios. For the latter a counteracting effect is observed in the early stages which somewhat disguises the true impact, and is revealed when comparing the cumulative turbine energy supply traces for the transients. Therefore, the effect that extrapolation has on the response prediction depends on the exact regions (left or right of the efficiency inflexion points) and the reduced speed coverage, of the transient in the map, and this is generally related to the starting engine power.

All the studied transients were characterized by an initial drop in turbine efficiency whilst the pressure ratio increased, corresponding to the "snap torque" of the engine. Depending on the initial and average compressor efficiency during this phase the turbine reduced speed may decrease substantially, and this determines how far away from the measured supplier data the remainder of the transient passes in the map. In this study it was found that this location can even fall outside the wide map data coverage. Finally, the cumulative turbine supply energy provides a very useful tool for comparing the impact of different types and levels of extrapolation on the transient simulation, and the final percentage differences in this variable are fairly well correlated with the observed differences in response time.

References

1. Jackson, N., Automotive Council The Digital Revolution – The Potential for Virtual Product Engineering in the Automotive Sector, 2016.
2. SAE, Turbocharger Gas Stand Test Code - J1826, 1995.
3. Watson, N., "Transient performance simulation and analysis of turbocharged diesel engines," *SAE Paper*, 1981.
4. Salameh, G., Chesse, P., and Chalet, D., "Experimental Study of Automotive Turbocharger Turbine Performance Maps Extrapolation," *SAE Technical Paper 2016-01-1034*, Detroit, MI, 2016, doi:10.4271/2016-01-1034.Copyright.
5. Hadef, J. El, Colin, G., Chamaillard, Y., and Talon, V., "Physical-Based Algorithms for Interpolation and Extrapolation of Turbocharger Data Maps," *SAE Int. J. Engines* 5(2):363–378, 2012, doi:10.4271/2012-01-0434.
6. Eriksson, L., "Modeling and Control of Turbocharged SI and DI Engines," *Oil Gas Sci. Technol. IFP* 62(4):523–538, 2008, doi:10.2516/ogst:2007042.
7. Jensen, J., Kristensen, A.F., Sorenson, S.C., and Houbak, N., "Mean Value Modeling of a Small Turbocharged Diesel Engine," *SAE Tech. Pap. 910070* 1–16, 1991, doi:10.4271/910070.
8. Martin, G., Talon, V., Peuchant, T., Higelin, P., and Charlet, A., "Physics based diesel turbocharger model for control purposes," *SAE Tech. Pap. 2009-24-0123*, 2009, doi:10.4271/2009-24-0123.
9. Watson, N. and Janota, M.S., "Turbocharging the Internal Combustion Engine," Wiley, ISBN 0471870722, 1982.
10. Benson, R.S., "The thermodynamics and gas dynamics of internal-combustion engines, vol. 1," Oxford University Press, ISBN 0 19 856210 1, 1982.
11. Payri, F., Serrano, J.R., Fajardo, P., Reyes-Belmonte, M.A., and Gozalbo-Belles, R., "A physically based methodology to extrapolate performance maps of radial turbines," *Energy Convers. Manag.* 55:149–163, 2012, doi:10.1016/j.enconman.2011.11.003.
12. Hadef, J. El, Colin, G., Talon, V., and Chamaillard, Y., "New physics-based turbocharger data-maps extrapolation algorithms: Validation on a spark-ignited engine," *IFAC Workshop on Engine and Powertrain Control, Simulation and Modelling (ECOSM)*, Rueil-Malmaison, France, ISBN 9783902823168: 213–220, 2012, doi:10.3182/20121023-3-FR-4025.00061.
13. Muñoz, M. and Payri, F., "Motores de Combustión Interna Alternativos," *Sección de Publicaciones de la E.T.S. de Ingenieros Industriales Fundación General – U.P.M, Madrid*, ISBN 84-86043-01-9, 1989.
14. Rautenberg, M. and Kammer, N., "On the Thermodynamics of Non Adiabatic Compression and Expansion in Turbomachines," *Proc. 5th International Conference for Mechanical Power Engineering*, Cairo, Egypt.
15. SAE, "Turbocharger Nomenclature and Terminology," *SAE International Surface Vehicle Recommended Practice*, SAE J922, 1995.
16. Szymko, S., Martinez-Botas, R.F., and Pullen, K.R., "Experimental evaluation of turbocharger turbine performance under pulsating flow conditions," *Proc ASME Turbo Expo No. GT2005-68878* 1–11, 2005, doi:10.1115/GT2005-68878.
17. Sanchez, T. and Muñoz, A., "Turbomáquinas Térmicas. Editorial Síntesis," ISBN 84-9756-185-6, 2004.
18. Seber, G.A.F. and Wild, C.J., "Nonlinear Regression," Wiley-Interscience, Hoboken, NJ, 2003.
19. Rakopoulos, C.D. and Giakoumis, E.G., "Diesel Engine Transient Operation: Principles of Operation and Simulation Analysis," Springer, 2009.
20. Caterpillar, Transient Test Creation Guide, 2010.
21. Gibson, D.H., "A Flexible Fuel Injection Simulation," *International Fuel and Lubricants Meeting and Exposition. SAE Paper No. 861567*, Philadelphia, Pennsylvania, 1986.
22. Sud, K., Cetinkunt, S., and Fiveland, S., "A simulation based comprehensive performance evaluation of Cat® C4.4 current production engine with its split cycle clean combustion variant using a validated one-dimensional modeling methodology," *SAE Technical Paper 2013-01-2434*, 2013, doi:10.4271/2013-01-2434.
23. Williams, D.R., Koci, C., and Fiveland, S., "Compression Ignition 6-Stroke Cycle Investigations," *SAE Int. J. Engines* 7(2):656–672, 2014, doi:10.4271/2014-01-1246.

24. Fluga, E.C., “Modeling of the Complete Vehicle Powertrain Using ENTERPRISE,” *SAE Technical Paper 931179*, 1–5, 1993, doi:10.4271/931179.

25. Ormistron, P., “Software simulates many disciplines in one model,” *Mach. Des. Mag.* Nov. 6, 2003.

Contact Information

Dr Aaron Costall
Imperial College London
Department of Mechanical Engineering
South Kensington Campus
London SW7 2AZ
UK

Email: a.costall@imperial.ac.uk

Acknowledgments

The authors would like to thank Caterpillar Inc. for their financial support and close technical collaboration on this work.

Disclaimer

Definitions

Roman symbols

$A_{\mathbf{eff}}$	effective area
A_0	volute flow cross section at tongue
C	flow velocity
c_p	specific heat capacity
D	diameter
h	enthalpy
I	rotational inertia (turbocharger)
$\dot{m}$	mass flow rate
$\overline{\dot{m}}$	non-dimensional mass flow rate
N	rotational speed
$\overline{N}$	fully reduced rotational speed
p	pressure
r	radius
R	gas constant
t	normalized time
U	rotor blade velocity
W	relative velocity
$\dot{W}$	power
$\overline{W}$	power absorption parameter

Greek symbols

τ	torque
γ	gas specific heats ratio
π	pressure ratio
η	efficiency
ν	blade speed ratio
ω	rotational speed
$\dot{\omega}$	rotational acceleration

Subscripts

0	total (stagnation)
1	rotor inlet
2	rotor outlet
a	air flow
c	compressor
is, **s**	isentropic
red	reduced
t	turbine
ts	total-to-static
wh	(turbine) wheel
θ	circumferential

Superscripts

test	from wide map test data
ref	reference supplier maps

Abbreviations

r.m.s.	root mean square
BSFC	brake specific fuel consumption
BSR	blade speed ratio
CSLA	constant speed load acceptance
IRF	inward radial flow
PCA	previous cycle averaged
PR	pressure ratio
SF	scale factor
SW	(typical) supplier width
TCS	torque converter stall
TIT	turbine inlet temperature
TR	transient response